

Local concentration focusing effect on deposition efficiency caused by inlet of fluids in MPCVD reactor

Zhiguo Tian, Bin Liu, Moran Wang *

Department of Engineering Mechanics and ASP, Tsinghua University, Beijing, 100084, China

ARTICLE INFO

Keywords:

MPCVD reactor
Diamond deposition
Multiphysical modeling
Local focusing

ABSTRACT

Microwave Plasma Chemical Vapor Deposition (MPCVD) has emerged as a prominent technique for advanced material synthesis, particularly diamond growth, characterized by inherently complex multiphysical phenomena. At moderate gas pressures (on the magnitude of 0.1 atmospheric pressure), flow effects play a substantial role in MPCVD reactors. However, most previous studies choose to neglect these flow characteristics due to huge computational challenges in multiphysical modeling. Empirical evidence has demonstrated that strategic modifications to fluid inlet configurations may enhance diamond deposition rates by an order of magnitude, yet the underlying mechanisms remain inadequately understood. This study implements a comprehensive multiphysical modeling framework incorporating coupled electromagnetic field, plasma field, flow field, and temperature field. Special attention is given to plasma characterization as a multi-component system requiring rigorous treatment through Maxwell–Stefan diffusion theory. However, previous theoretical analysis reveals a critical limitation in conventional Maxwell–Stefan implementations, which is the inherent assumption of inviscid flow. This contradicts the viscous nature of MPCVD operational environments, as evidenced by our simulation results, demonstrating the necessity of viscous diffusion integration in heavy species transport to achieve experimental consistency. The inclusion of viscous diffusion mechanisms reveals enhanced hydrogen atom concentration near substrate apertures through inlet-induced flow modifications. This concentration enhancement directly correlates with improved deposition rates as per the Goodwin–Harris model. Our findings establish that viscous diffusion constitutes a previously overlooked yet critical transport mechanism in MPCVD reactors, complementing conventional mass diffusion and convective transport. This revelation provides new fundamental insights into diamond deposition mechanisms and proposes a novel process optimization paradigm through transport manipulation.

1. Introduction

Microwave Plasma Chemical Vapor Deposition (MPCVD) has established itself as a preeminent technique for synthesizing advanced functional materials, particularly diamond and graphene. Diamond emerges as the most strategically significant material in this context due to its exceptional combination of bulk properties: supreme mechanical hardness, wide bandgap width, exceptional charge carrier mobility, and unmatched thermal conductivity. These extraordinary attributes collectively position diamond as the “ultimate semiconductor” material, with our study specifically focusing on its synthesis via MPCVD technology.

The seminal achievement of diamond synthesis using MPCVD dates back to the 1980s [1]. Over subsequent decades, MPCVD has evolved into the dominant methodology for producing large-scale, high-purity diamond, surpassing conventional High Pressure High Temperature (HPHT) approaches in both quality and scalability. Contemporary

MPCVD systems exhibit diverse reactor configurations when classified according to chamber geometry, including cylindrical [2], quartz bell-jar [3], ellipsoidal [2], butterfly [4], and multi-slot designs [5,6]. Parallel advancements in process optimization have been achieved through innovations in growth parameter control [7,8]. Nevertheless, a persistent challenge remains — current MPCVD technology yields diamond wafers with maximum diameters constrained to approximately 10 cm, significantly below the dimensional requirements for practical semiconductor device fabrication. This critical limitation underscores the need for fundamental advances in plasma physics understanding and multiphysical process optimization to enable next-generation diamond synthesis breakthroughs.

The scientific framework for understanding MPCVD centers on two fundamental challenges: (i) identifying critical species governing diamond growth and (ii) elucidating dominant transport mechanisms for

* Corresponding author.

E-mail address: mrwang@tsinghua.edu.cn (M. Wang).

<https://doi.org/10.1016/j.diamond.2025.112840>

Received 26 May 2025; Received in revised form 4 September 2025; Accepted 15 September 2025

Available online 19 September 2025

0925-9635/© 2025 Elsevier B.V. All rights are reserved, including those for text and data mining, AI training, and similar technologies.

these species. While the precursor gas mixture (typically H_2 and CH_4) appears chemically simple, plasma dissociation generates a complex array of reactive intermediates through electron-impact and thermal reactions, often numbering in the hundreds. This chemical complexity necessitates rigorous discrimination of kinetically relevant species. Hydrogen atoms were first established as pivotal growth mediators through parallel discoveries by U.S. and Soviet researchers [9–13]. The Goodwin–Harris model [14,15] formalized this understanding by reducing diamond deposition to five dominant surface reactions, expressing growth rates as an explicit function of hydrogen atom concentration. Experimental validation across diverse conditions [16] has solidified consensus on hydrogen's mechanistic primacy. While hydrogen's role as a growth precursor is undisputed, the interplay of competing transport mechanisms remains inadequately resolved. This ambiguity hinders predictive control over deposition uniformity at industrial scales.

MPCVD reactor constitutes a quintessential multiphysics system involving electromagnetic fields, plasma dynamics, thermal transport, and fluid mechanics coupled. Species transports within this environment is governed by synergistic interactions between these physical domains. A critical scientific challenge arises from the inherent invisibility of species-specific transport phenomena and the practical impossibility of direct experimental observation. Recent advances in multiphysical simulations have partially mitigated this limitation, enabling detailed visualization of species distributions [2,16–24]. Of particular significance is the substantial influence of flow dynamics on plasma behavior under the characteristic pressure regime of MPCVD ($\sim 10^4$ Pa). Emerging computational studies [25–27] have begun elucidating this interaction through conventional Advection–Diffusion–Reaction (ADR) formulations for heavy species transport. However, experimental anomalies reported by Zhao et al. [28,29] challenge this paradigm: introducing a secondary substrate-centered gas inlet (10 SCCM CH_4) while maintaining primary H_2 flow (500 SCCM) through the upper chamber enhances deposition rates by an order of magnitude. The Goodwin–Harris model attributes this enhancement to elevated hydrogen atom density near the substrate surface, implying modified transport physics. This phenomenon defies ADR-based predictions, as the minimal CH_4 flow through the auxiliary inlet cannot account for observed plasma modifications under conventional transport assumptions. The discrepancy reveals fundamental limitations in current theoretical frameworks, suggesting the existence of unaccounted transport mechanisms governing plasma-phase species redistribution.

To address this discrepancy, a rigorous re-examination of the Advection–Diffusion–Reaction (ADR) framework is essential. From a fundamental perspective, the H_2 – CH_4 plasma constitutes a multi-component gas mixture whose diffusion dynamics are theoretically governed by the Maxwell–Stefan model. This framework, which constitutes a generalized formulation extending the Fick's law, derives rigorously from three distinct theoretical foundations: hydrodynamic principles [30], kinetic gas theory [31], and nonequilibrium thermodynamics [32]. However, as critically noted by Lam [33], the standard Maxwell–Stefan derivation inherently assumes inviscid flow conditions — a simplification incompatible with viscous transport phenomena prevalent in MPCVD environments. For viscous flow regimes, the model requires augmentation through an additional term accounting for viscous momentum transfer during inter-species interactions [33]. In this study, we implement a modified Maxwell–Stefan formulation incorporating viscous diffusion effects within a fully-coupled multiphysical modeling framework. This advancement enables resolution of previously intractable experimental anomalies, particularly those involving localized flow perturbations with disproportionate impacts on deposition kinetics.

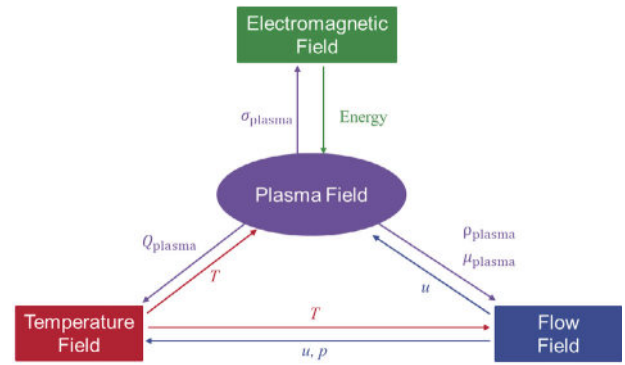


Fig. 1. Multiphysics simulation framework.

2. Method and equations

The multiphysical modeling framework adopted in this work is demonstrated as Fig. 1. Electromagnetic field, plasma field, temperature field, and flow field are fully coupled, among which some physical parameters are transferred self-consistently. In the following part, how these four fields are simulated and the definitions of the transferred parameters are introduced in sequence.

2.1. Electromagnetic field

First of all, in MPCVD, the microwave provides energy input for the whole system. To obtain the electromagnetic field, the Maxwell's equations need to be solved:

$$\begin{cases} \nabla \times \vec{H} = \sigma_{em} \vec{E} + \frac{\partial(\epsilon_{em} \vec{E})}{\partial t}, \\ \nabla \times \vec{E} = -\frac{\partial(\mu_{em} \vec{H})}{\partial t}, \\ \nabla \cdot (\epsilon_{em} \vec{E}) = -e \sum_{\alpha} Z_{\alpha} n_{\alpha}, \\ \nabla \cdot (\mu_{em} \vec{H}) = 0, \end{cases} \quad (1)$$

where \vec{E} is electric field vector, \vec{H} is magnetic field vector, ϵ_{em} is the permittivity, μ_{em} is the permeability, σ_{em} is the electrical conductivity, e is the charge of an electron, and $\sum_{\alpha} Z_{\alpha} n_{\alpha}$ represents the sum of the charges of all cations, anions, and electrons. This equation set can be re-arranged into frequency domain form, or Helmholtz equation, as:

$$\nabla \times (\mu_r^{-1} (\nabla \times \vec{E})) + (j\omega\sigma_{plasma} - \omega^2\epsilon_r) \vec{E} = 0, \quad (2)$$

where \vec{E} is the amplitude of electric field, j is the imaginary unit, ϵ_r is the relative permittivity, μ_r is the relative permeability and ω is the microwave frequency, $\omega = 2.45$ GHz in the present work. σ_{plasma} is the conductivity of the plasma, whose expression is [34]:

$$\sigma_{plasma} = \frac{e^2 n_e}{m_e (v_e + j\omega)}, \quad (3)$$

where n_e is the number density of electron, m_e is the electron mass, and v_e is the effective collision frequency of electron. The boundary condition for Eq. (2) is ideal conductor wall, $\vec{n}_b \times \vec{E} = 0$, where \vec{n}_b is the normal vector for the wall.

The input microwave energy can heat the plasma through the Ohmic heating:

$$Q_{plasma} = \frac{1}{2} \text{Re} [\sigma_{plasma} \vec{E} \cdot \vec{E}^*] = \frac{e^2 n_e v_e |\vec{E}|^2}{2m_e (v_e^2 + \omega^2)}, \quad (4)$$

where the symbol Re means taking the real part, and \vec{E}^* is the conjugate vector of the electric field. Eq. (4) acts as the source term in the following heat transfer equation for the plasma temperature.

Furthermore, to maintain the quasi-neutrality of the plasma, the Poisson's equation is involved:

$$-\nabla \cdot \epsilon_{em} \nabla V = e \left(\sum_k Z_k n_k - n_e \right), \quad (5)$$

where V is the electric potential. The boundary condition for this Poisson's equation is $V = 0$, which means that the walls are treated as ground.

2.2. Plasma field

After this, the plasma field needs to be simulated. The calculation of the plasma field includes two main parts: the electron transport and the heavy species transport.

2.2.1. Electron transport

For the electron transport, the drift-diffusion equations [35] should be adopted:

$$\begin{cases} \frac{\partial n_e}{\partial t} + \nabla \cdot \Gamma_e + (\vec{u} \cdot \nabla) n_e = R_e, \\ \Gamma_e = -(\mu_e \cdot \vec{E}) n_e - \nabla (\bar{D}_e n_e), \\ \frac{\partial n_e}{\partial t} + \nabla \cdot \Gamma_e + \vec{E} \cdot \Gamma_e + (\vec{u} \cdot \nabla) n_e = S_{en} + (Q + Q_{gen})/e, \\ \Gamma_e = -(\mu_e \cdot \vec{E}) n_e - \nabla (\bar{D}_e n_e), \end{cases} \quad (6)$$

where Γ_e is the electron flux vector, R_e is electron rate expression, μ_e is the electron mobility, \bar{D}_e is the electron diffusivity, n_e is the electron energy density, Γ_e is the electron energy density flux vector, S_{en} is the energy loss/gain due to inelastic collisions, Q is an external heat source, Q_{gen} is a generalized heat source, μ_e is the electron energy mobility, and \bar{D}_e is the electron energy diffusivity. \vec{u}_g is the mass averaged fluid velocity vector which is calculated as $\vec{u}_g = \frac{\sum_k \rho_k \vec{u}_k}{\sum_k \rho_k}$. The electron rate expression and inelastic energy loss/gain are calculated as:

$$R_e = \sum_1^M x_j k_j N_n n_e, \quad (7)$$

$$S_{en} = \sum_1^P x_j k_j N_n n_e \Delta \epsilon_j, \quad (8)$$

where x_j is the mole fraction of the target species for reaction j , k_j is the rate coefficient for reaction j , N_n is the total neutral number density, M is the total number of the electron impact reactions, $\Delta \epsilon_j$ is the energy loss from reaction j , and P is the total number of the inelastic reactions. The rate coefficient is calculated as:

$$k_j = \sqrt{\frac{2e}{m_e}} \int_0^\infty \epsilon \sigma_j(\epsilon) f(\epsilon) d\epsilon, \quad (9)$$

where ϵ is the electron energy, $\sigma_j(\epsilon)$ is the collision cross section for reaction j , and $f(\epsilon)$ is the Electron Energy Distribution Function (EEDF). The generalized EEDF is:

$$f(\epsilon) = g \varphi^{-3/2} \beta_1 \exp(-(\epsilon \beta_2 / \varphi)^g), \quad (10)$$

where $\beta_1 = \Gamma(5/(2g))^{3/2} \Gamma(3/(2g))^{-5/2}$, $\beta_2 = \Gamma(5/(2g)) \Gamma(3/(2g))^{-1}$, Γ is the Gamma function, and g is a constant, $1 \leq g \leq 2$. When $g = 1$, Eq. (10) stands for the Maxwellian EEDF. Therefore, the electron temperature T_e and the mean electron energy $\bar{\epsilon}$ is obtained as: $T_e = 2\bar{\epsilon}/3$, $\bar{\epsilon} = n_e/n_e$. The boundary conditions for Eqs. (6) are $\vec{n}_b \cdot \Gamma_e = \frac{1}{2} v_{e,th} n_e$, $\vec{n}_b \cdot \Gamma_e = \frac{5}{6} v_{e,th} n_e$, where $v_{e,th}$ is the electron thermal velocity, whose expression is $v_{e,th} = \sqrt{\frac{8k_B T_e}{\pi m_e}}$.

The above electron transport equations requires data input, that is the electron impact cross section. In the present work, we only consider hydrogen molecules, due to the fact that in the gas mixture of MPCVD, the volume ratio of the hydrogen molecules is over 90% and hydrogen molecules are capable of representing the overall behavior of

Table 1
Electron impact reactions.

Reaction	Formula	Type
R1	$e + H \Rightarrow e + H$	Elastic
R2	$e + H \Rightarrow e + H^*$	Excitation
R3	$e + H \Rightarrow e + Hn2$	Excitation
R4	$e + H \Rightarrow e + Hn3$	Excitation
R5	$e + H \Rightarrow 2e + H^+$	Ionization
R6	$e + H_2 \Rightarrow e + H_2$	Elastic
R7	$e + H_2 \Rightarrow e + H_2(v = 1)$	Vibrational excitation
R8	$e + H_2 \Rightarrow e + H_2(v = 2)$	Vibrational excitation
R9	$e + H_2 \Rightarrow e + H_2(v = 3)$	Vibrational excitation
R10	$e + H_2 \Rightarrow e + H + Hn2$	Dissociative excitation
R11	$e + H_2 \Rightarrow e + H + Hn3$	Dissociative excitation
R12	$e + H_2 \Rightarrow e + H + H$	Dissociation
R13	$e + H_2 \Rightarrow 2e + H_2^+$	Ionization
R14	$e + H_2 \Rightarrow 2e + H + H^+$	Ionization
R15	$e + H_3^+ \Rightarrow 3H$	Recombination
R16	$e + H_2^+ \Rightarrow H_2 + Hn2$	Recombination
R17	$e + H_2^+ \Rightarrow H + Hn2$	Recombination
R18	$e + H_2^+ \Rightarrow H + Hn3$	Recombination

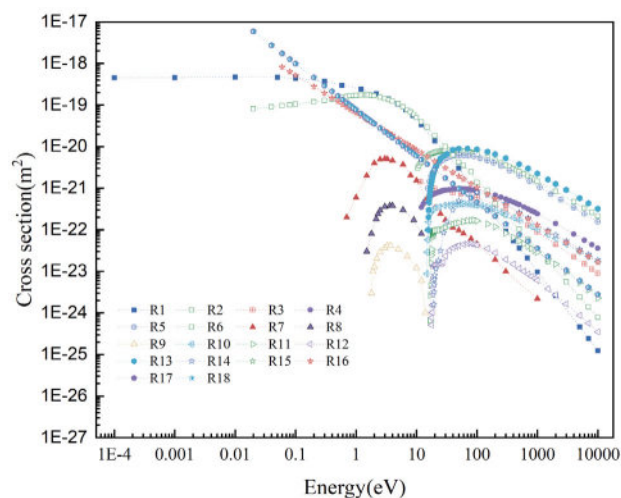


Fig. 2. Electron impact reactions cross section.

Table 2
Arrhenius form reaction.

Reaction	Formula	Reaction rate ($m^3 s^{-1} mol^{-1}$)
R19	$e + H^+ \Rightarrow Hn2$	$1.81 \times 10^4 (T_{plasma}/1[K])^{-0.5}$
R20	$e + H^+ \Rightarrow Hn3$	$1.81 \times 10^4 (T_{plasma}/1[K])^{-0.5}$
R21	$H_2 + Hn2 \Rightarrow e + H_3^+$	$6.02 \times 10^6 (T_{plasma}/1[K])^{0.5}$
R22	$H_2 + Hn3 \Rightarrow e + H_3^+$	$6.02 \times 10^6 (T_{plasma}/1[K])^{0.5}$
R23	$H_2 + H^+ \Rightarrow H + H_3^+$	1.26×10^9
R24	$H_2 + H_2 \Rightarrow 2H + H_2$	$2.23 \times 10^8 \cdot e^{-48300[K]/T_{plasma}}$
R25	$2H + H_2 \Rightarrow H_2 + H_2$	$3.02 \times 10^8 (300[K]/T_{plasma})$
R26	$H_2 + H \Rightarrow 3H$	$2.23 \times 10^8 \cdot e^{-48300[K]/T_{plasma}}$
R27	$3H \Rightarrow H_2 + H$	$3.02 \times 10^8 (300[K]/T_{plasma})$

the plasma [16,20]. Because methane and related carbon chemistry are not included, the model neglects methane depletion and the subsequent formation of higher hydrocarbons. For hydrogen plasma, 8 kinds of species, including e, H_2 , H, Hn2 (the excited state of hydrogen atom corresponding to the level $n = 2$), Hn3 (the excited state of hydrogen atom corresponding to the level $n = 3$), H^+ , H_2^+ , H_3^+ and 27 reactions are included, as listed in Tables 1 and 2. The electron impact reactions cross sections are plotted out in Fig. 2. This reaction set is consistent with previous studies [16,20] and the data for these reactions are from [36–41]. Additionally, the EEDF is assumed to be Maxwellian EEDF and the Local Energy Approximation is adopted. Electron temperature is obtained from the electron energy equation.

Table 3
Surface reactions.

Reaction	Formula	Reaction sticking coefficient
S1	H => 0.5H ₂	0.02
S2	Hn2 => H	1
S3	Hn3 => H	1
S4	H ⁺ => H	1
S5	H ₂ ⁺ => H ₂	1
S6	H ₃ ⁺ => H + H ₂	1

2.2.2. Heavy species transport

The heavy species (except for the electron *e*) transport is the most concerned in this work. Traditionally, the Advection–Diffusion–Reaction (ADR) equation is adopted in previous numerical work [4,19,25–27], whose form is:

$$\frac{\partial n_k}{\partial t} + \nabla \cdot (n_k \vec{u}_g) + \nabla \cdot (-D_{k,m} \nabla n_k) = R_k, \quad (11)$$

where n_k is the number density of species k , $D_{k,m}$ is the mixture averaged diffusion coefficient of species k , and R_k is the rate expression for species k . Eq. (11) is derived by combining the mass conservation law and the Maxwell–Stefan model, which constitutes a generalized formulation extending the Fick's law. Here, we demonstrate the derivation process because it is directly related to the novelty of the present work. The mass conservation is expressed as:

$$\frac{\partial n_k}{\partial t} + \nabla \cdot (n_k \vec{u}_k) = R_k, \quad (12)$$

where \vec{u}_k is the velocity of species k . \vec{u}_k can be decomposed as $\vec{u}_k = \vec{u}_g + \vec{u}_d$, where \vec{u}_d is the diffusion velocity of species k . This diffusion velocity can be assumed to be linearly related to its concentration gradient, which is specifically the Maxwell–Stefan model:

$$\vec{u}_d = -D_{k,m} \nabla n_k. \quad (13)$$

Substituting Eq. (13) and $\vec{u}_k = \vec{u}_g + \vec{u}_d$ into Eq. (12), the traditional ADR Eq. (11) can be derived.

One important thing to be discussed is the assumptions of the Maxwell–Stefan model. Actually, the Maxwell–Stefan model for multi-component diffusion can be theoretically deduced from macroscopic hydrodynamic equations [30], kinetic gas theory [31], or thermodynamics [32] independently. These derivations have pointed out that the dynamics of the gas mixture had been assumed to be inviscid. If this inviscid assumption is to be relaxed, an additional term needs to be added to the classical law [33]:

$$\vec{u}_d = -D_k \nabla n_k - \gamma_k \nabla^2 \vec{u}_g, \quad (14)$$

where $\gamma_k = \frac{\mu_k}{m_k \nu_k}$ stands for the number of collisions per meter. μ_k , m_k , and ν_k are the dynamic viscosity, mass, and effective collision rate of species k . Eq. (14) accounts for the viscous diffusion in the viscous flow. While Fickian diffusion arises from molecular thermal motion, the viscous diffusion term represents the entrainment of radicals by externally imposed pressure/velocity gradients, including inlet and outlet effects; it is applied to all heavy species, and ion-slip is negligible under present conditions. Quantitative comparison between these two terms, mass diffusion and viscous diffusion, can be performed as:

$$\frac{\mathcal{O}(\gamma_k \nabla^2 u_g)}{\mathcal{O}(D_{k,m} \nabla n_k)} \sim \frac{\frac{\mu_k}{m_k \nu_k} \frac{U}{L^2}}{D_{k,m} \frac{N}{L}} \sim \frac{\mu_k}{\rho_k D_{k,m}} \frac{1/\nu_k}{L/U} = \frac{Sc}{Da}, \quad (15)$$

where Sc and Da are the dimensionless numbers, Schmidt number and Damköhler number respectively, which govern the key transport mechanisms in MPCVD reactors, defined respectively as: $Sc = \frac{\mu_k}{\rho_k D_{k,m}}$ and $Da = \frac{L/U}{1/\nu_k}$. Sc stands for the ratio of viscous diffusion rate and mass diffusion rate. Da represents the ratio between the flow timescale and the reaction timescale. Considering hydrogen atoms in MPCVD systems as a representative case, characteristic values of these parameters reveal

critical insights. Da typically exceeds unity across most reactor domains, though reduced values emerge near inlet/outlet regions due to (i) enhanced characteristic velocities and (ii) suppressed reaction rates under these boundary flow conditions. For multi-component diffusion, Sc would also much larger than 1, due to hydrogen's exceptionally low mass density combined with comparable magnitudes of μ_k and $D_{k,m}$ — a consequence of their shared \sqrt{T} temperature dependence. This scaling analysis demonstrates that viscous diffusion effects attain comparable significance to mass diffusion in the MPCVD environments, necessitating their inclusion in transport models. Our numerical simulations confirm elevated Sc / Da ratios (>1) near flow boundaries, as shown in subsequent sections. To address these physics, we implement a modified formulation (14) describing viscous-mass coupled diffusion, which when integrated into the continuity Eq. (12) yields:

$$\frac{\partial n_k}{\partial t} + \nabla \cdot (n_k \vec{u}_g) + \nabla \cdot (-D_{k,m} \nabla n_k - \gamma_k \nabla^2 u_g) = R_k. \quad (16)$$

Eq. (16) incorporates the viscous diffusion into the traditional ADR equation. In the following simulation, H₂, H, Hn2, Hn3, H⁺, H₂⁺, and H₃⁺ are solved with Eq. (16), and the Poisson's equation is solved to maintain overall charge neutrality. A set of surface reactions in Table 3 are implemented as the boundary conditions for describing the loss/gain of these heavy species on the walls.

2.3. Flow field

In MPCVD reactors, the temperature can be as high as 3000 K and there also exists lots of reactions, which cause density variation. Therefore, although the flow velocity is much smaller than sonic velocity, the compressible Navier–Stokes equations are adopted to capture the density fluctuation [42]:

$$\frac{\partial \rho_g}{\partial t} + \nabla \cdot (\rho_g \vec{u}_g) = 0, \quad (17)$$

$$\rho_g \frac{\partial \vec{u}_g}{\partial t} + \rho_g \vec{u}_g \cdot \nabla \vec{u}_g = -\nabla p + \nabla \cdot \left(\mu \left(\nabla \vec{u}_g + (\nabla \vec{u}_g)^T \right) - \frac{2}{3} \mu \left(\nabla \cdot \vec{u}_g \right) \vec{I} \right) + \vec{F}, \quad (18)$$

where ρ_g , μ , and \vec{u}_g are the mass density, dynamic viscosity, and velocity of the gas mixture, \vec{F} is the external force which is 0 in this work which means the gravity force is not included. Non-slip boundary conditions are applied for Eqs. (17) and (18).

2.4. Temperature field

The heat transfer equation is solved [42]:

$$\rho_g C_p \frac{\partial T_{\text{plasma}}}{\partial t} + \rho_g C_p \vec{u}_g \cdot \nabla T_{\text{plasma}} = \kappa \cdot \nabla T_{\text{plasma}} + Q_{\text{plasma}}, \quad (19)$$

where C_p is the specific heat capacity at constant pressure, T_{plasma} is the plasma temperature, κ is the thermal conductivity, and Q_{plasma} is calculated from Eq. (4). The boundary conditions for Eq. (19) are: the substrate temperature is kept at 1200 K and all other walls are assigned by convective heat transfer condition with heat transfer coefficient of 200 W/(m² K) and external temperature as 300 K. That is because: (i) 1200 K is a typical diamond growth temperature [16,20]; (ii) all other walls are cooled by circulating water.

All the equations and boundary conditions are implemented in the COMSOL Multiphysics, a commercial computational platform based on the Finite Element method. The simulation domain is 2D axisymmetric structure. It takes approximately 30 min to complete one case computation by using a computer with i7-12700F CPU and 32 GB RAM. Transient simulations are advanced from 0 s to 100 s; the upper limit is sufficient for the solution to reach steady state. Adequate mesh refinement in the plasma region is applied to guarantee convergence.

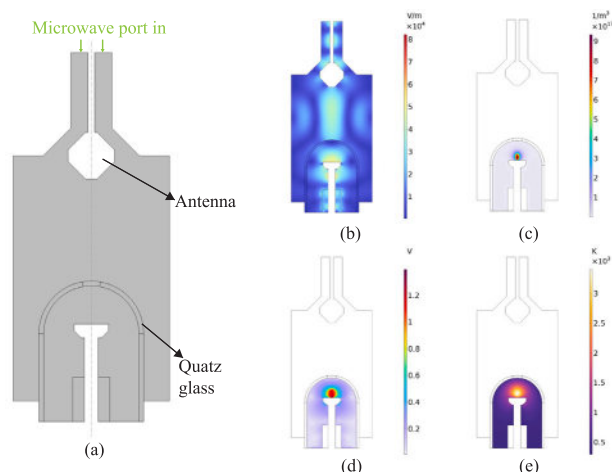


Fig. 3. Benchmark geometry and simulation results for hydrogen only in 500 W and 25 000 Pa: (a) geometry, similar as in [16,20]; (b) electric field; (c) electron number density; (d) electron temperature; (e) plasma temperature. This simulation does not include the flow field.

3. Code verification and benchmarks

To validate our computational framework, we reproduce seminal contributions in MPCVD modeling by Hassouni et al. [20] and Hassouni et al. [16], selected for their widespread adoption in the field and availability of experimental validation data. A geometrically equivalent reactor configuration, as Fig. 3(a) shows, was implemented, with simulations performed at 500 W power and 25,000 Pa pressure. The radius of the substrate area is 25 mm. First of all, the mesh independence is implemented and the results are demonstrated in Appendix B. As shown in Fig. 3(b)–(e), the spatial distributions of plasma properties exhibit qualitative consistency with reference results [16,20] in both morphology and relative intensity.

For quantitative validation, Fig. 4 compares key metrics across four operational conditions: 600 W, 2500 Pa; 1000 W 5200 Pa; 1500 W, 8400 Pa; 2000 W, 11 000 Pa, respectively. Our simulated maximum plasma temperatures and hydrogen atomic mole fractions (solid markers) fall within the range bounded by prior computational results and experimental measurements from [20]. The small discrepancy most likely arises from two sources: (i) the reaction set employed here is both a simplification of the real chemistry and differs slightly from that used by Hassouni et al. [20]; (ii) the actual reactor is three-dimensional, whereas our model is axisymmetric, so three-dimensional effects inevitably introduce additional deviations. This multi-fidelity agreement confirms our framework's capability to capture the essential physics in MPCVD. Notably, these validation cases intentionally exclude flow field effects to isolate plasma-specific behavior, consistent with the baseline assumptions of the referenced studies. Subsequent sections introduce viscous flow coupling to address unresolved transport anomalies.

4. Results and discussion

Following rigorous code validation, we investigate flow-plasma coupling effects through parametric studies of inlet velocity and geometric configurations.

4.1. Influence of high velocity

The interplay between elevated flow velocities and plasma dynamics has been theoretically predicted [14] and computationally demonstrated [25–27]. To systematically characterize this relationship, five flow regimes were simulated with inlet mass flow rates spanning

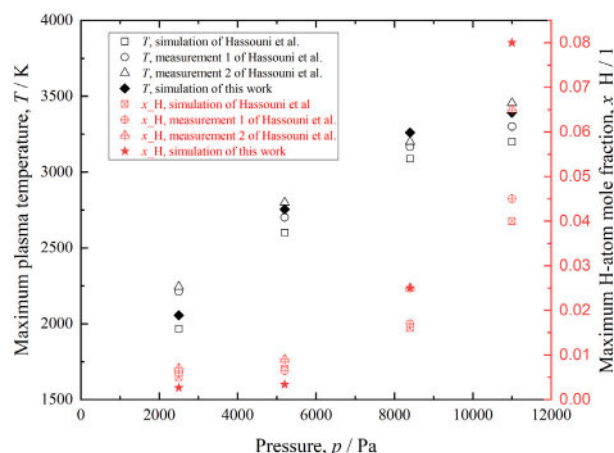


Fig. 4. Quantitative comparisons with results in [20]. The working conditions for the four cases are: 600 W, 2500 Pa; 1000 W 5200 Pa; 1500 W, 8400 Pa; 2000 W, 11 000 Pa. These simulation do not include the flow field.

400–10 000 SCCM, as Fig. 5 demonstrates. Velocity streamlines, hydrogen atom number density, and plasma temperature distributions were analyzed using the conventional Advection–Diffusion–Reaction formulation (Eq. (11)) to maintain methodological consistency with prior studies [25–27]. Key observations include: (i) flow transition: vortex formation initiates at 2000 SCCM, becoming pronounced above 4500 SCCM; (ii) plasma suppression: increased advection reduces hydrogen atom density and lowers peak plasma temperatures across the parameter space; (iii) threshold behavior: significant velocity effects emerge only above 2000 SCCM. These results align with Goodwin's theory [14], where enhanced flow rates accelerate species removal from the deposition zone. However, under standard MPCVD operating conditions (<1000 SCCM), velocity magnitudes remain insufficient to perturb plasma distributions. This explains why conventional ADR models suffice for typical flow regimes while failing under auxiliary inlet configurations that induce localized high-velocity anomalies.

4.2. Influence of inlet design

Except for high velocity effect, some experimental measurements have demonstrated that by only changing the inlet design, the deposition process can be strongly affected. This experimental phenomenon cannot be explained by the high velocity influence since the inlet flow rate is kept at about 500 SCCM in the experiment, far away from 2000 SCCM as has been discussed in Fig. 5. To uncover the underlying mechanism, Eq. (16) is incorporated into the simulation. The following part will present the main simulation results.

Fig. 6 presents our cylindrical reactor geometry, replicating the experimental configuration of Zhao et al. [29] for direct comparability. The substrate radius is 50 mm. The simulation results, including the electric field, the electron number density, the electron temperature, and the plasma temperature, vividly prove that this MPCVD apparatus works well. Then, four different inlets are designed, as shown in Fig. 6. In these four cases, the flow inlet 1 and the outlet are kept as the same. Besides, the flow inlet 1 is above the platform and its flow rate is kept at 500 SCCM, which is also the same as the experiment in the paper [29]. An additional inlet, gas inlet 2, is added in the center of the platform and this is also similar as the experimental design in the paper [29]. The flow rates of gas inlet 2, Q_s , are designed as 0, 10, 20, and 30 SCCM respectively. Fig. 6 demonstrates the flow field in contour and the flow streamline by using the radial velocity and the axial velocity in arrow. With the increase of Q_s , the velocity near the platform surface increases.

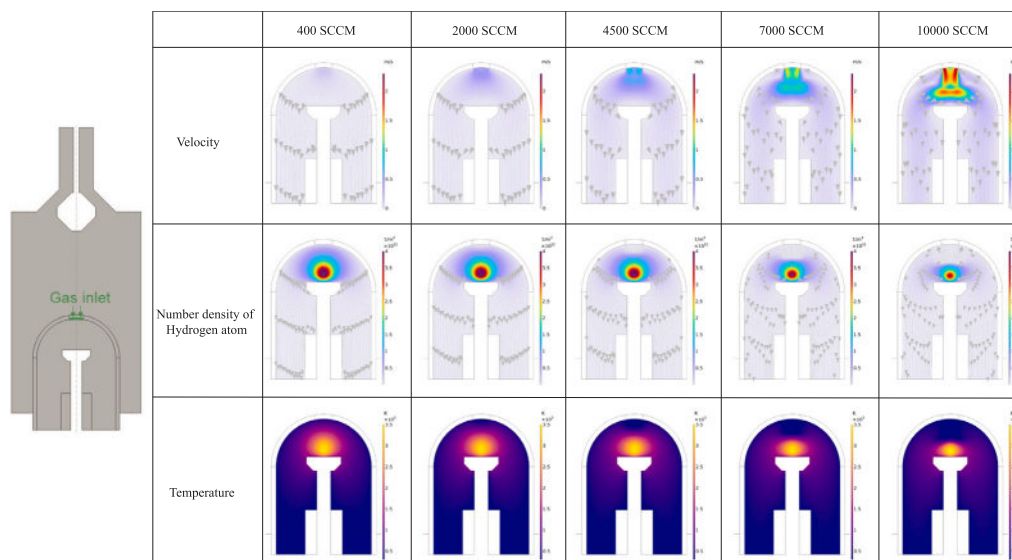


Fig. 5. Influence of high velocity. Five cases with different inlet flow rates are simulated: 400, 2000, 4500, 7000, 10 000 SCCM, respectively. The flow velocity, number density of hydrogen atom, and plasma temperature are plotted with velocity streamline.

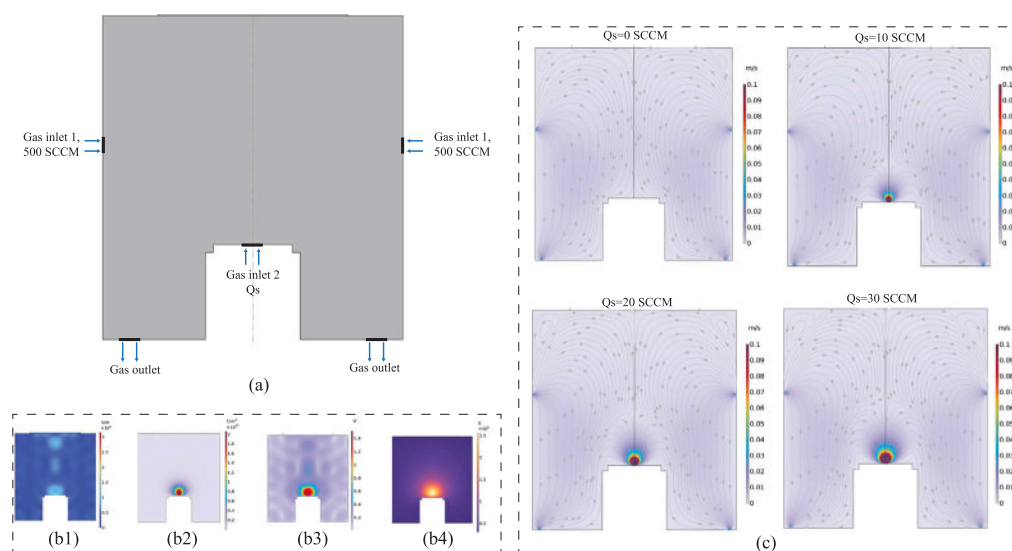


Fig. 6. Simulation geometry and flow designs: (a) basic geometry; (b) simulation results for hydrogen in 500 W and 5000 Pa without flow field, (b1)–(b4) are electric field, electron number density, electron temperature, and plasma temperature, respectively; (c) flow designs: the rate of gas inlet 1 in the upper side is kept at 500 SCCM and only the rate of the gas inlet 2 in the center of the platform is changed. Four different cases are designed, in which Q_s is 0, 10, 20, 30 SCCM. The velocity magnitude is presented in contour and the velocity streamline, which is plotted by using the radial and axial velocity, is demonstrated in arrows.

Fig. 7 demonstrates the spatial distribution of hydrogen atom without and with viscous diffusion for the designed four cases. In Fig. 7, the contour is the number density of hydrogen atom and the arrow is the velocity streamline, which is plotted by using the radial and axial velocity. The upper row in Fig. 7 is the results without viscous effect, by Eq. (11), which presents that there is no difference for the four cases. That means the traditional ADR equation is not capable of grasping experimental measurements in the paper [29]. On the contrary, if the viscous diffusion is taken into consideration, by adopting Eq. (16), the simulation results (the lower panels in Fig. 7) show that the number density of the hydrogen atom near the platform hole increases with the flow rate Q_s . In the referenced experiments [29] methane and nitrogen are supplied through the susceptor, whereas hydrogen is introduced on the top. During the tens of hours required for diamond growth,

the reactor is continuously purged, so the background methane and nitrogen concentrations become spatially uniform before any significant deposition occurs. Under these conditions any local rise in hydrocarbon precursors is governed by transport and not by fresh gas injection. Fig. 7 supports this view: removing viscous diffusion eliminates the radial peak in H-atom density. Because the same transport mechanism (viscous diffusion + convection) governs all neutral species, the absence of a small amount of methane and nitrogen injected from the substrate center does not invalidate the conclusion that viscous diffusion is responsible for the observed radial enhancement of the growth rate.

To quantitatively illustrate the simulation results, two monitoring lines are chosen: a horizontal one on the surface and a vertical one in the symmetrical axis, as shown in Fig. 8. For the vertical line, the axial position 0 means the platform surface. It shows that when Q_s

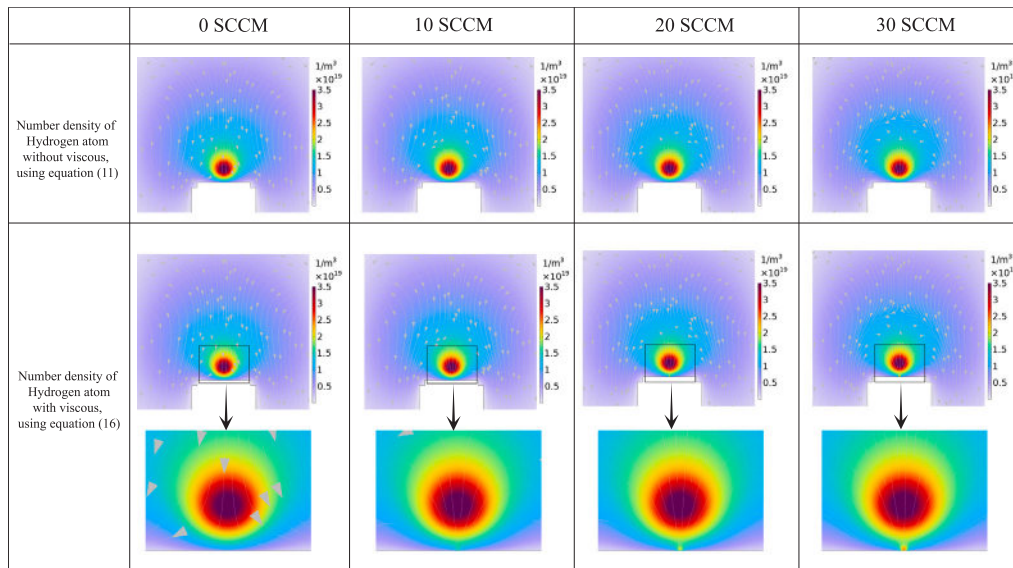


Fig. 7. Spatial distributions of hydrogen atom without and with viscous effect for the four different cases. The number density of hydrogen atom is presented in contour and the velocity streamline, by plotting the radial and axial velocity, is in arrows.

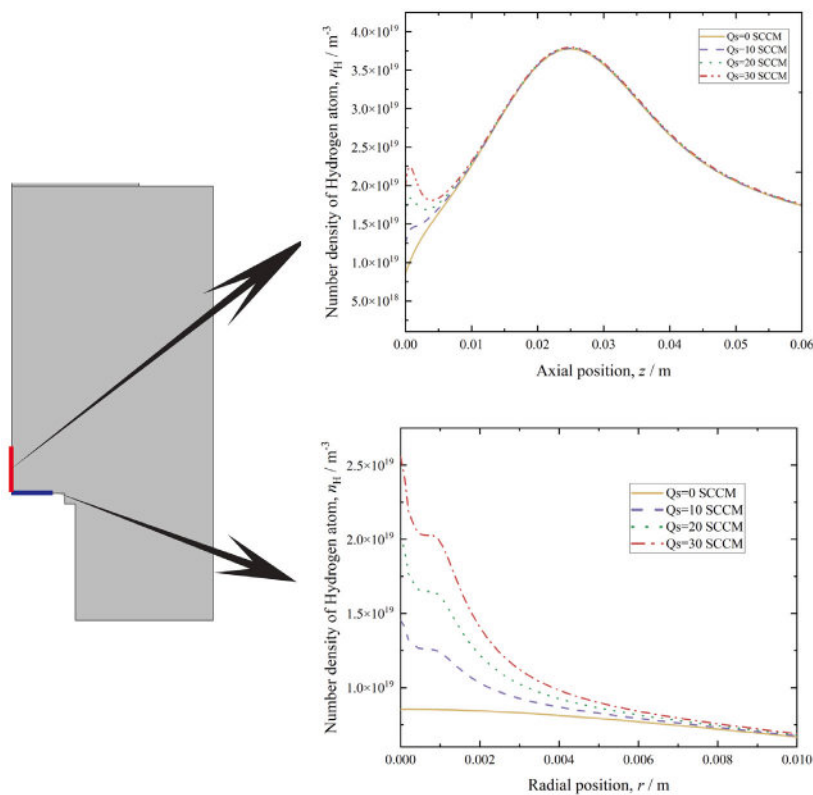


Fig. 8. Number density of hydrogen atom on two monitoring lines: a horizontal one on the surface and a vertical one in the symmetrical axis.

is 0 SCCM, which equals that there is no platform hole, the number density of hydrogen atom is non-monotonic with one local peak. After the introduction of the platform hole, the other three cases present two local peaks, with an additional one near the surface. For the horizontal monitoring line, it shows that the hydrogen atom increases with the flow rate of the platform hole. According to the Goodwin–Harris model, the focusing of hydrogen atom near the substrate surface directly contribute to the increase of the deposition rate. In other words, these

simulation results proves that the increases of the deposition rate in the experiments [29] should be caused by the viscous momentum transfer.

4.3. Mechanistic analysis

The physical origin of observed deposition enhancements is quantified through dimensionless analysis in Fig. 9. As derived in formula (15), the relative significance of viscous versus mass diffusion is governed by the ratio Sc/Da , where $Sc = \frac{\mu_k}{\rho_k D_{k,m}}$ is the Schmidt number

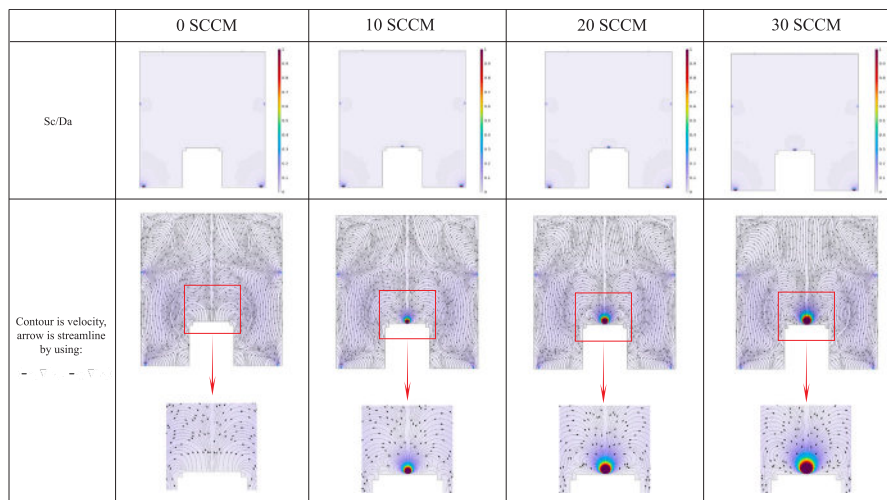


Fig. 9. Spatial distributions of Sc/Da , Eq. (15), and streamline by using $(-\gamma_k \nabla^2 u_r, -\gamma_k \nabla^2 u_z)$, where u_r is the radial velocity and u_z is the axial velocity. Such streamlines vividly demonstrate the entrainment effect of the fluid inlet after introducing the viscous momentum transfer for heavy species transport, Eq. (16).

and $Da = \frac{L/U}{1/\nu_k}$ is the Damköhler number respectively. Sc stands for the ratio of viscous diffusion rate and mass diffusion rate, which is explicitly calculated during the simulation, shown in Appendix. Da represents the ratio of the flow timescale and the reaction timescale. The effective collision rate, ν_k can be estimated as $\nu_k = \frac{k_b T}{m D_{k,m}}$ from kinetic theory. Spatial mapping of Sc/Da (Fig. 9) reveals distinct transport regimes: (i) boundary zones (inlet/outlet regions): $Sc/Da > 1$ (viscous diffusion dominant); (ii) bulk plasma region: $Sc/Da \ll 1$ (mass diffusion dominant). This bifurcation is visualized through viscous momentum streamlines $(-\gamma_k \nabla^2 u_r, -\gamma_k \nabla^2 u_z)$ in Fig. 9. Without auxiliary flow ($Q_s = 0$), streamline dispersion indicates weak viscous coupling. Introduction of the substrate inlet ($Q_s > 0$) induces focusing near the surface. The mechanistic sequence emerges: auxiliary flow perturbs velocity gradients near substrates; enhanced viscous stresses amplify momentum coupled diffusion; modified transport redistributes hydrogen radicals to surface-proximal regions; deposition kinetics accelerate per Goodwin–Harris dependencies. This framework reconciles the experimental paradox — minor flow additions achieve disproportionate effects by the viscous diffusion transport physics rather than the bulk flow advection.

5. Conclusions

This work conducts multiphysical simulations in a MPCVD reactor, in which the electromagnetic field, plasma field, flow field, and temperature field are simultaneously calculated. Given the hydrogen dominant mass fraction (>90%) in diamond deposition process in MPCVD reactors, we employ a hydrogen-dominated plasma approximation to balance computational efficiency with physical fidelity — a validated approach in the prior studies. The critical theoretical advancement lies in reforming heavy species transport modeling. Theoretical derivations of the Maxwell–Stefan diffusion model for multi-component gas mixture, based on hydrodynamic equations, kinetic gas theory, or thermodynamics, have been proved to assume the gas mixture to be inviscid and the species should be dilute. However, for MPCVD, the gas pressure is on the magnitude of 0.1 atmospheric pressure and thus the flow of the hydrogen molecule should be viscous. Moreover, the dissociation of the hydrogen molecule increases with the microwave power and reaches almost 10% for general MPCVD working conditions, which means that the species is not dilute anymore. Therefore, in the present work, the viscous diffusion is introduced to describe the heavy species behavior, besides mass diffusion and convection. By doing this, the local concentration focusing caused by the fluid inlet

is observed in the simulation and the numerical results we obtained are not contradictory with the preceding experimental findings, although we acknowledge that our model may underestimate the inlet effect by omitting hydrocarbon chemistry. The validated framework explains the order-of-magnitude deposition improvements reported experimentally, attributing them to viscous momentum transfer rather than pure advective effects. Quantitative validation remains challenging for two reasons: sparse experimental data and the absence of methane chemistry in our current model. All in all, this mechanistic insight establishes flow geometry optimization as a new MPCVD control dimension, complementing traditional power/pressure adjustments.

CRediT authorship contribution statement

Zhiguo Tian: Writing – original draft, Validation, Investigation, Data curation. **Bin Liu:** Software, Resources, Data curation. **Moran Wang:** Writing – review & editing, Supervision, Investigation, Conceptualization.

Declaration of competing interest

The authors declare that they have no known competing financial interests or personal relationships that could have appeared to influence the work reported in this paper.

Acknowledgments

This work was financially supported by the National Natural Science Foundation of China (No. 12432013, 12272207) and the Tsinghua University Initiative Scientific Research Program.

Appendix A. Physical parameters calculation

In the appendix, the calculation of the physical parameters in the multiphysics simulation is presented.

The mixture averaged diffusion coefficient of species k , $D_{k,m}$ is:

$$D_{k,m} = \frac{1 - w_k}{\sum_1 x_j / D_{kj}}, \quad (\text{A.1})$$

where w_k is the mass fraction of species k , x_k is the mole fraction of species k , and D_{kj} is the binary diffusion coefficient between species

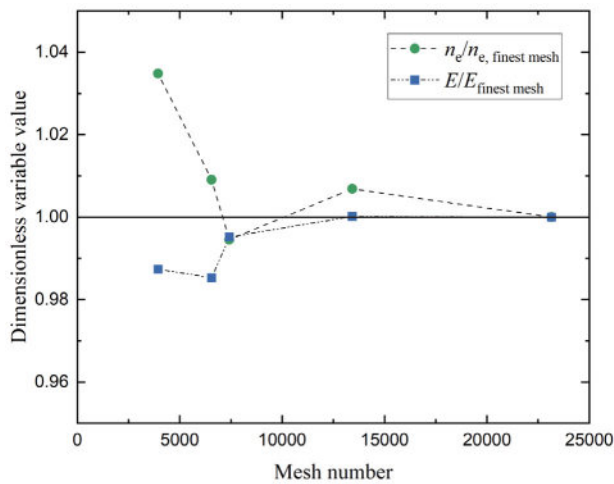


Fig. B.10. Mesh independence test results. 5 different meshes are generated with mesh number as 3946, 6557, 7419, 13 421, and 23 435. A point, which is 10 mm above the center of the platform, is monitored. Different variables, including the electron number density n_e and electric field amplitude E are recorded and presented by dimensionless variables, which are calculated by dividing the value with the one of the finest mesh, 23 435.

k and j . The binary diffusion coefficients, D_{kj} , are computed based on kinetic gas theory [43,44], as:

$$D_{kj} = 0.0266 \frac{\sqrt{T^3 (M_k + M_j) / (2000 M_k M_j)}}{p \sigma_{kj}^2 \Omega_D}, \quad (\text{A.2})$$

where M_k is the molecular weight of species k , T is the gas temperature, p is the gas pressure, σ is the characteristic length of the Lennard-Jones potential and Ω_D is the collision integral for diffusion coefficient. Ω_D is very complex and can be approximated in the following form at moderate pressure:

$$\Omega_D = A (T^*)^{-B} + C [\exp(-DT^*)] + E [\exp(-FT^*)] + G [\exp(-HT^*)] + \frac{0.19 \delta_{kj}^2}{T^*}, \quad (\text{A.3})$$

where $T^* = k_b \frac{T}{\sqrt{\epsilon_k \epsilon_j}}$, $\sigma_{kj}^2 = \left(\frac{\sigma_k + \sigma_j}{2} \right)^2$, $\delta = \frac{1}{2} \frac{\zeta^2}{\epsilon \sigma^3}$, ζ is the species dipole moment.

The dynamic viscosity can be calculated by kinetic theory [43,44] as:

$$\mu_i = 2.67 \cdot 10^{-6} \frac{\sqrt{1000 T M_i}}{\sigma_i^2 \Omega_v}, \quad (\text{A.4})$$

where Ω_v is the collision integral for dynamic viscosity, which is estimated as:

$$\Omega_v = A (T^*)^{-B} + C [\exp(-DT^*)] + E [\exp(-FT^*)] + \frac{0.20 \delta^2}{T^*}. \quad (\text{A.5})$$

Appendix B. Mesh independence test

A mesh-independence study for Fig. 3 is summarized in Fig. B.10. The dimensionless difference between successive refinements monotonically decreases, converging to unity with minor oscillations. Consequently, the grid with 7 419 elements is selected for all results reported in Fig. 3.

Data availability

The data that has been used is confidential.

References

- [1] M. Kamo, H. Yurimoto, Y. Sato, Epitaxial growth of diamond on diamond substrate by plasma assisted CVD, *Appl. Surf. Sci.* 33 (1988) 553–560.
- [2] M. Funer, C. Wild, P. Koidl, Simulation and development of optimized microwave plasma reactors for diamond deposition, *Surf. Coat. Technol.* 116 (1999) 853–862.
- [3] K. Hassouni, O. Leroy, S. Farhat, A. Gicquel, Modeling of H 2 and H 2/CH 4 moderate-pressure microwave plasma used for diamond deposition, *Plasma Chem. Plasma Process.* 18 (1998) 325–362.
- [4] H. Yamada, A. Chayahara, Y. Mokuno, S.-i. Shikata, Model of reactive microwave plasma discharge for growth of single-crystal diamond, *Japan. J. Appl. Phys.* 50 (1S1) (2011) 01AB02.
- [5] F. Silva, K. Hassouni, X. Bonnin, A. Gicquel, Microwave engineering of plasma-assisted CVD reactors for diamond deposition, *J. Phys.: Condens. Matter.* 21 (36) (2009) 364202.
- [6] Z. Zhai, C. Zhang, B. Chen, Y. Xiong, Y. Liang, L. Liu, B. Yang, N. Yang, X. Jiang, N. Huang, Covalently-Bonded diaphite nanoplatelet with engineered electronic properties of Diamond, *Adv. Funct. Mater.* (2024) 2401949.
- [7] S.-W. Kim, R. Takaya, S. Hirano, M. Kasu, Two-inch high-quality (001) diamond heteroepitaxial growth on sapphire (1120) misoriented substrate by step-flow mode, *Appl. Phys. Express* 14 (11) (2021) 115501.
- [8] V. Uwhireye, Y. Hu, G. Cao, X. Zhang, F.E. Oropeza, K.H. Zhang, Recent progress on heteroepitaxial growth of single crystal diamond films, *Electron* 2 (4) (2024) e70.
- [9] J.C. Angus, H.A. Will, W.S. Stanko, Growth of diamond seed crystals by vapor deposition, *J. Appl. Phys.* 39 (6) (1968) 2915–2922.
- [10] B. Spitsyn, L. Bouilov, B. Derjaguin, Vapor growth of diamond on diamond and other surfaces, *J. Cryst. Growth* 52 (1981) 219–226.
- [11] R. DeVries, Synthesis of diamond under metastable conditions, *Annu. Rev. Mater. Sci.* 17 (1) (1987) 161–187.
- [12] W.A. Yarbrough, R. Messier, Current issues and problems in the chemical vapor deposition of diamond, *Science* 247 (4943) (1990) 688–696.
- [13] J.C. Angus, Diamond synthesis by chemical vapor deposition: The early years, *Diam. Relat. Mater.* 49 (2014) 77–86.
- [14] D.G. Goodwin, Scaling laws for diamond chemical-vapor deposition. I. Diamond surface chemistry, *J. Appl. Phys.* 74 (11) (1993) 6888–6894.
- [15] D. Goodwin, Scaling laws for diamond chemical-vapor deposition. II. Atomic hydrogen transport, *J. Appl. Phys.* 74 (11) (1993) 6895–6906.
- [16] K. Hassouni, F. Silva, A. Gicquel, Modelling of diamond deposition microwave cavity generated plasmas, *J. Phys. D: Appl. Phys.* 43 (15) (2010) 153001.
- [17] M. Funer, C. Wild, P. Koidl, Numerical simulations of microwave plasma reactors for diamond CVD, *Surf. Coat. Technol.* 74 (1995) 221–226.
- [18] E. Pleuler, C. Wild, M. Funer, P. Koidl, The CAP-reactor, a novel microwave CVD system for diamond deposition, *Diam. Relat. Mater.* 11 (3–6) (2002) 467–471.
- [19] H. Yamada, A. Chayahara, Y. Mokuno, Simplified description of microwave plasma discharge for chemical vapor deposition of diamond, *J. Appl. Phys.* 101 (6) (2007).
- [20] K. Hassouni, T. Grotjohn, A. Gicquel, Self-consistent microwave field and plasma discharge simulations for a moderate pressure hydrogen discharge reactor, *J. Appl. Phys.* 86 (1) (1999) 134–151.
- [21] Y.A. Mankelevich, M.N. Ashfold, J. Ma, Plasma-chemical processes in microwave plasma-enhanced chemical vapor deposition reactors operating with C/H/Ar gas mixtures, *J. Appl. Phys.* 104 (11) (2008).
- [22] M.N. Ashfold, Y.A. Mankelevich, Self-consistent modeling of microwave activated N2/CH4/H2 (and N2/H2) plasmas relevant to diamond chemical vapor deposition, *Plasma Sources Sci. Technol.* 31 (3) (2022) 035005.
- [23] M.N. Ashfold, Y.A. Mankelevich, Two-dimensional modeling of diamond growth by microwave plasma activated chemical vapor deposition: Effects of pressure, absorbed power and the beneficial role of nitrogen on diamond growth, *Diam. Relat. Mater.* 137 (2023) 110097.
- [24] G. Wang, Y. Hu, X. Li, C. Yin, H. Zhu, Y. Yang, Multiphysics simulation study in a microwave plasma reactor coupling a non-maxwellian EEDF, *Plasma Sources Sci. Technol.* 33 (11) (2024) 115019.
- [25] A. Mesbahi, F. Silva, S. Farhat, K. Hassouni, X. Bonnin, A. Gicquel, Hydrodynamics effects in high power density microwave plasma diamond growth reactors, *J. Phys. D: Appl. Phys.* 46 (38) (2013) 385502.
- [26] S. Prasanna, C. Rond, A. Michau, K. Hassouni, A. Gicquel, Effect of buoyancy on power deposition in microwave cavity hydrogen plasma source, *Plasma Sources Sci. Technol.* 25 (4) (2016) 045017.
- [27] A. Mesbahi, F. Silva, Study of the influence of gas flow on PECVD diamond growth: influence of the separate injection of gases, *J. Phys. D: Appl. Phys.* 50 (47) (2017) 475203.
- [28] W. Zhao, Y. Teng, K. Tang, S. Zhu, K. Yang, J. Duan, Y. Huang, Z. Chen, J. Ye, S. Gu, Significant suppression of residual nitrogen incorporation in diamond film with a novel susceptor geometry employed in MPCVD, *Chin. Phys. B* 31 (11) (2022) 118102.
- [29] W. Zhao, Y. Teng, K. Tang, S. Zhu, D. Liu, K. Yang, J. Duan, Y. Huang, Z. Chen, J. Ye, et al., An innovative gas inlet design in a microwave plasma chemical vapor deposition chamber for high-quality, high-speed, and high-efficiency diamond growth, *J. Phys. D: Appl. Phys.* 56 (37) (2023) 375104.

- [30] F.A. Williams, Elementary derivation of the multicomponent diffusion equation, *Am. J. Phys.* 26 (467–469) (1958) 312.
- [31] W.H. Furry, On the elementary explanation of diffusion phenomena in gases, *Am. J. Phys.* 16 (2) (1948) 63–78.
- [32] C. Curtiss, R.B. Bird, Multicomponent diffusion, *Ind. Eng. Chem. Res.* 38 (7) (1999) 2515–2522.
- [33] S. Lam, Multicomponent diffusion revisited, *Phys. Fluids* 18 (7) (2006).
- [34] G. Hagelaar, K. Hassouni, A. Gicquel, Interaction between the electromagnetic fields and the plasma in a microwave plasma reactor, *J. Appl. Phys.* 96 (4) (2004) 1819–1828.
- [35] E. Gogolides, H.H. Sawin, Continuum modeling of radio-frequency glow discharges. I. Theory and results for electropositive and electronegative gases, *J. Appl. Phys.* 72 (9) (1992) 3971–3987.
- [36] L. Marques, J. Jolly, L. Alves, Capacitively coupled radio-frequency hydrogen discharges: The role of kinetics, *J. Appl. Phys.* 102 (6) (2007).
- [37] M. Capitelli, C.M. Ferreira, B.F. Gordiets, A.I. Osipov, *Plasma Kinetics in Atmospheric Gases*, vol. 31, Springer Science & Business Media, 2013.
- [38] R. Janev, W. Langer, K. Evans Jr., D. Post Jr., *Elementary Processes in Hydrogen-Helium Plasmas*, in: *Atoms and Plasmas*, Vol. 4, 1987.
- [39] S. Pancheshnyi, S. Biagi, M.-C. Bordage, G. Hagelaar, W. Morgan, A. Phelps, L.C. Pitchford, The LXCat project: Electron scattering cross sections and swarm parameters for low temperature plasma modeling, *Chem. Phys.* 398 (2012) 148–153.
- [40] L.C. Pitchford, L.L. Alves, K. Bartschat, S.F. Biagi, M.-C. Bordage, I. Bray, C.E. Brion, M.J. Brunger, L. Campbell, A. Chachereau, et al., Lxcat: An open-access, web-based platform for data needed for modeling low temperature plasmas, *Plasma Process. Polym.* 14 (1–2) (2017) 1600098.
- [41] E. Carbone, W. Graef, G. Hagelaar, D. Boer, M.M. Hopkins, J.C. Stephens, B.T. Yee, S. Pancheshnyi, J. Van Dijk, L. Pitchford, Data needs for modeling low-temperature non-equilibrium plasmas: the LXCat project, history, perspectives and a tutorial, *Atoms* 9 (1) (2021) 16.
- [42] T.L. Bergman, *Fundamentals of Heat and Mass Transfer*, John Wiley & Sons, 2011.
- [43] P.D. Neufeld, A. Janzen, R. Aziz, Empirical equations to calculate 16 of the transport collision integrals $\Omega(l, s)^*$ for the Lennard-Jones (12–6) potential, *J. Chem. Phys.* 57 (3) (1972) 1100–1102.
- [44] R.S. Brokaw, Predicting transport properties of dilute gases, *Ind. Eng. Chem. Process. Des. Dev.* 8 (2) (1969) 240–253.